Liquid Crystal Elastomer–Liquid Metal Composite: Ultrafast, Untethered, and Programmable Actuation by Induction Heating

Victor Maurin, Yilong Chang, Qiji Ze, Sophie Leanza, Jing Wang, and Ruike Renee Zhao*

Liquid crystal elastomers (LCEs) are a class of stimuli-responsive materials that have been intensively studied for applications including artificial muscles, shape morphing structures, and soft robotics due to their capability of large, programmable, and fully reversible actuation strains. To fully take advantage of LCEs, rapid, untethered, and programmable actuation methods are highly desirable. Here, a liquid crystal elastomer-liquid metal (LCE-LM) composite is reported, which enables ultrafast and programmable actuations by eddy current induction heating. The composite consists of LM sandwiched between two LCE layers printed via direct ink writing (DIW). When subjected to a high-frequency alternating magnetic field, the composite is actuated in milliseconds. By moving the magnetic field, the eddy current is spatially controlled for selective actuation. Additionally, sequential actuation is achievable by programming the LM thickness distribution in a sample. With these capabilities, the LCE-LM composite is further exploited for multimodal deformation of a pop-up structure, on-ground omnidirectional robotic motion, and in-water targeted object manipulation and crawling.

1. Introduction

Stimuli-responsive materials capable of altering their shape and physical properties in response to external stimulations, such as magnetic field, light, or heat, have enabled a range of novel soft robotic capabilities, including adaptive motion in extreme and unpredictable environments,[1,2] reconfigurable electronics,[3–5] and biomedical devices.[6–8] Examples of stimuli-responsive materials include shape memory polymers,[4,9–11] hydrogels,[12–14] soft magnetic polymers,[15–17] and liquid crystal elastomers (LCEs).[18–20] LCEs have been extensively explored to develop artificial muscles,[21,22] shape morphing structures,[23–25] and soft robots[26,27] due to their capability of generating large, programmable, and fully reversible actuation strains typically up to 40–50% under temperature change.[28] When an LCE is heated above its transition temperature, a nematic-to-isotropic phase transition is triggered, inducing a microstructural rearrangement of its liquid crystals (or mesogens) from an aligned state to a disorganized state, producing a macroscopic contraction along the mesogen alignment direction.[29] Upon cooling, the mesogens regain their alignment and the LCE recovers its original length. With this effective thermo-mechanical response, LCEs are capable of generating fully reversible and large shape changes,[28] as well as high energy density deformations.[30]

To drive the thermal actuation of LCEs, joule heating,[3,31,32] photothermal heating,[33–35] heat guns,[36] hot plates,[25] and hot water baths[37] have been used. Among these methods, joule heating has been widely utilized to program the heating distribution in LCE structures for desired shape morphing by embedding resistance heating components such as electric heating wires and pads at the prescribed locations in the LCE.[38] Although joule heating has enabled intricate LCE structure actuation, this method is tethered, which hinders LCE applications in constrained or enclosed environments where tethered wire system access is undesired or limited. For methods using heat guns, hot plates, and hot water baths, the temperature of the whole sample is increased at once, allowing for only a single deformation mode.[25,36,37] Even though photothermal heating can achieve more localized energy transmission for selective actuation, it also has limitations when considering actuation environments that are inaccessible by light.[39]

Alternatively, induction heating is a promising untethered strategy for rapid temperature increase of materials. It uses high-frequency magnetic fields and can be integrated with LCEs for untethered and programmable heating, which permits LCE actuation in constrained or enclosed environments due to the ability of magnetic fields to penetrate through objects. In general, there are two induction heating mechanisms, namely hysteresis loss and eddy current. Hysteresis loss converts the energy loss from the magnetization and demagnetization cycle of ferromagnetic materials to produce heat. The heating of soft materials through hysteresis loss is usually implemented through embedding magnetic particles, such as iron oxide particles, in a soft polymer matrix.[4,40–42] However, this method has obvious drawbacks due to its limited heating efficiency, the significant increase in

V. Maurin, Y. Chang, Q. Ze, S. Leanza, J. Wang, R. R. Zhao
Department of Mechanical Engineering
Stanford University
Stanford, CA 94305, USA
E-mail: rrzhao@stanford.edu

**ADVANCED
SCIENCE NEWS**

www.advancedsciencenews.com

**ADVANCED
MATERIALS**

www.advmat.de

polymer stiffness, and the potential destruction of the polymer chain alignment during fabrication, which hinder LCE actuation.[43,44] In comparison, eddy current generates heat through the electrical current induced in a conductive material under a changing magnetic field. Considering liquid metal (LM)[45] as the conductive material for induction heating of thermal-responsive soft materials such as LCEs, tremendous advantages are offered due to the ultrafast heating for rapid actuation, along with the large strains of the soft system enabled by LM's negligible stiffness.

In this work, we report a novel liquid crystal elastomer-liquid metal (LCE-LM) composite which allows for ultrafast, untethered, and highly programmable actuation through eddy current induction heating. The composite consists of LM sandwiched between two 3D-printed LCE layers. The LCEs are printed via direct ink writing (DIW) and thus their actuated configurations can be controlled through the printing pathway.[36,46,47] The LM is sprayed onto a mask, which allows for programmable LM patterns.[48–50] The eddy current heating efficiency can be regulated by the thickness of LM, which is quantified by the number of LM layers sprayed. When subjected to a high-frequency alternating magnetic field, the composite can be actuated in milliseconds. By moving the magnetic field, the eddy current can be spatially controlled to enable selective actuation. Additionally, sequential heating is achievable by programming the LM thickness distribution. The LCE-LM composite, together with the 3D printing design capabilities offered by DIW, are further exploited for multimodal deformation of a pop-up structure, on-ground omnidirectional robotic motion, in-water targeted object manipulation, and in-water crawling. This work presents a novel way for ultrafast and programmable actuation of LCEs for applications where untethered control is highly desirable.

2. Results and Discussions

2.1. LCE-LM Composite Design and Fabrication

In this section, the LCE-LM composite is first described. The fabricated composite (**Figure 1**A) is composed of LM sandwiched between two LCE layers which are 3D-printed via DIW (see "Experimental Section" for the LCE ink and printing parameters). The printed LCE has a measured shear modulus of 507 kPa at the actuation temperature of 120 °C (see Figure S1, Supporting Information, for the material characterizations). As illustrated in Figure 1B, to allow for programmable shape morphing, the LCE mesogens are aligned through the shear stress generated during the extrusion of the LCE fibers from the print nozzle. The LCE actuation can be designed by programming the DIW print path. The printed layers are cured with UV light. The LM is then sprayed on top of the printed LCE via a mask, which allows for different LM patterns (Figure 1B). Another printed LCE layer is cured with UV light and placed on top to cover the LM. The whole structure is then cured together under UV light (see "Experimental Section" and Figure S2,Supporting Information, for more details on the LCE-LM composite fabrication, see Figure S3, Supporting Information, for the interfacial adhesion characterization of the composite). When a high-frequency alternating magnetic field is applied perpendicular to the LM pattern, an ohmic loss is generated through eddy current (Figure 1C, see "Experimental

Section" for induction heating details). The temperature can increase to over 120 °C (40% LCE strain, see Figure S1, Supporting Information, for the strain versus temperature curve of the LCE) in milliseconds, during which the LCE transitions from its nematic state to isotropic state for ultrafast and large contraction due to LM's negligible stiffness. When cooled, the LCE recovers back to its nematic state and original length (Figure 1D). By designing the LM pattern on the LCE layer, the actuation is effectively programmed. As illustrated in Figure 1E, an LCE disk is printed with circumferentially aligned mesogens and an LM ring is positioned concentric with the LCE disk. When a magnetic field of magnitude $B = 107.4$ mT and frequency $f = 37$ kHz (see Figures S4–S8, Supporting Information, for more details on the coils used in this paper) is applied, the outer edges of the disk deform within 0.4 s and bend upward into a flower-like shape. When the LM pattern is programmed as a concentric LM circle, the sample pops up into a hat-like shape within 1 s (Figure 1F, see Movie S1, Supporting Information, for the LCE disk deformations, see "Experimental Section" for details on the disk fabrication). Utilizing this untethered, programmable, and fast heating strategy, we further exploit LCE-LM composites to enable sequential and selective actuation for various functions including multimodal deformation, on-ground, and in-water robotic motion.

2.2. Characterizations of LM Induction Heating

The heat generated by the induction heating of LM is determined by the LM pattern geometry, thickness, as well as magnetic field intensity and frequency. In this section, the induction heating efficiency of LM is first characterized by heating LM squares of the same size (15 mm × 15 mm) but with different thicknesses. Note that the thickness of LM is controlled by the number of coatings sprayed, denominated as "layers", with a single layer being ∼10 μm thick (see Figure S9, Supporting Information, for the relationship between the thickness and the number of LM layers sprayed). As depicted in **Figure 2**A, an LM square with 10 layers (∼100 μm thick) is first heated under a nearly uniform magnetic field with $B = 41.1$ mT and $f = 51$ kHz (see Figure S5, Supporting Information, for coil details). The temperature distribution recorded by IR imaging agrees with the simulated ohmic loss distribution predicted by finite element analysis (FEA), indicating higher temperatures at the edges due to the skin effect induced by the high-frequency alternating magnetic field[51,52] (see Movie S2, Supporting Information, for the heating process of the LM square, and Supporting Information for the electromagnetic FEA). As shown in Figure 2B, the total ohmic loss increases nearly linearly with the thickness under the same alternating magnetic field. In Figure 2C, it is observed that the heating speed increases with the number of LM layers. To actuate the LCE, 100 °C provides a 30% contraction strain (see Figure S1, Supporting Information, for the strain versus temperature curve of the LCE). With 8-layer LM (∼80 μm thick), the temperature increases to above 100 °C in less than 1 s. With 30-layer LM (∼300 μm thick), it reaches 100 °C in less than 0.3 s.

Induction heating makes on-demand selective actuation easily achievable by changing the location of the electromagnetic
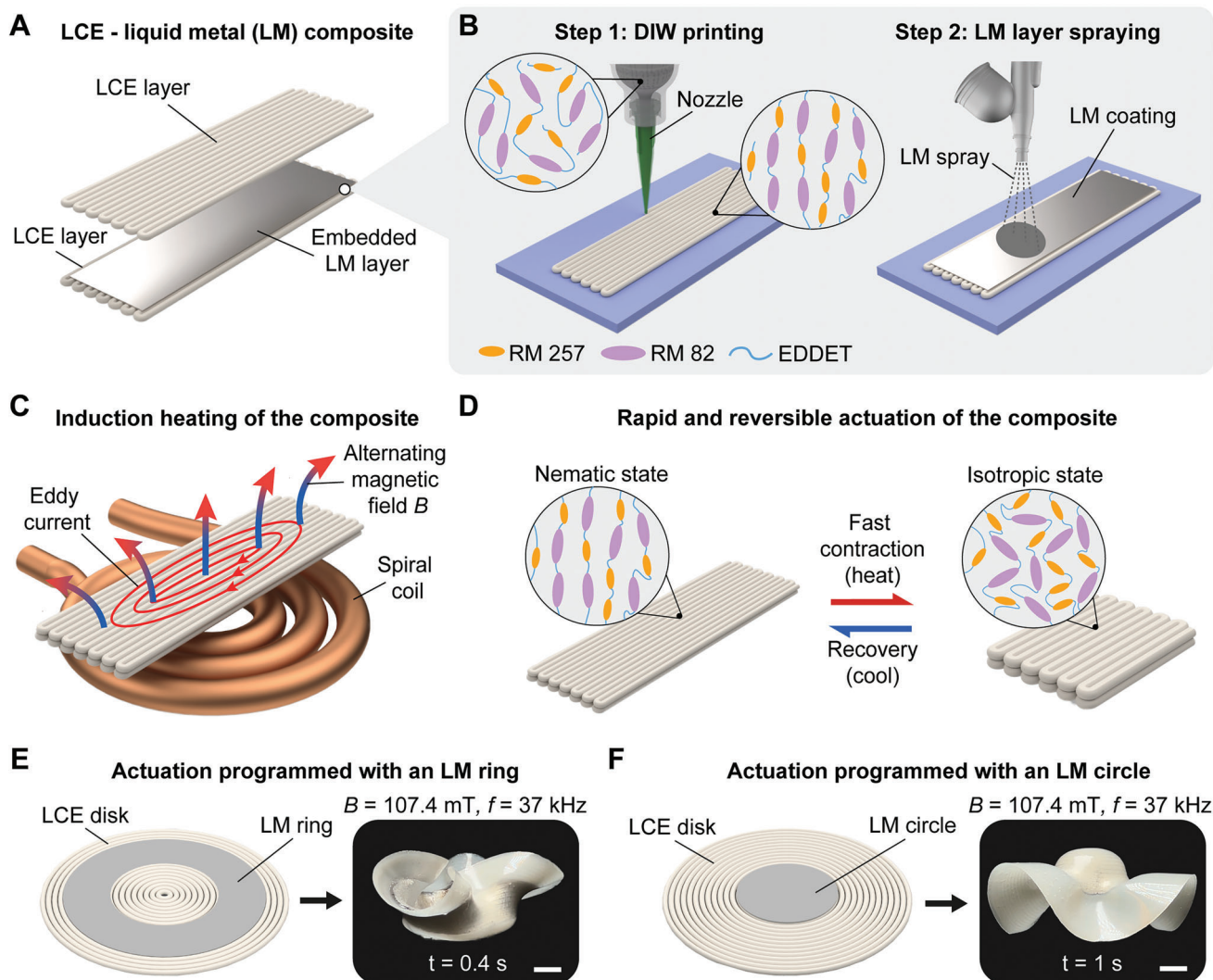
**ADVANCED
SCIENCE NEWS**

www.advancedsciencenews.com

**ADVANCED
MATERIALS**

www.advmat.de

Figure 1. LCE-LM composite fabrication, induction heating mechanism, and programmed actuations via designed LM patterns. A) Exploded view of the LCE-LM composite consisting of LM sandwiched between two LCE layers. B) DIW printing of the LCE layer and LM spraying. The mesogens are aligned along the print path. C) Schematic for induction heating of the composite, where a high-frequency alternating magnetic field induces eddy currents in the LM. D) Schematic of rapid contraction (heating of the composite) and recovery (cooling of the composite). Schematics and programmed actuated state with $B = 107.4$ mT and $f = 37$ kHz of E) an LCE disk with a concentric LM ring on the disk surface and F) an LCE disk with a concentric LM circle on the disk surface. The LCE disks have circumferential alignment direction. Scale bars: 5 mm.

coil. As illustrated in Figure 2D, a smaller spiral coil (see Figure S6, Supporting Information, for coil details) is used to generate a concentrated alternating magnetic field with $B = 152.8$ mT and $f = 46$ kHz. By placing the coil at three distinct positions, localized heating occurs in these targeted regions which is demonstrated by heating the two 7-layer (~70 μm thick) LM squares at different locations (see Movie S2, Supporting Information, for the selective heating of the LM squares). The temperature distribution recorded by IR imaging is accurately predicted by the simulated ohmic loss distribution. When the coil is placed at position 1, concentrated heating occurs only in the top LM square, and no heating is observed in the bottom LM square. When the coil is moved to position 2, between the two squares, the heating is concentrated at the edges of the two LM squares. Finally, at position 3, heating is only observed for the bot-

tom LM square, whereas no heating is observed for the top LM square.

Additionally, since the induction heating speed is proportional to the number of LM layers, sequential actuation is feasible by gradually increasing the magnetic field in regions with different numbers of LM layers. To demonstrate this, three LM squares with varied thicknesses are sequentially heated above 120 °C inside a helical coil (see Figure S7, Supporting Information, for coil details) at different magnetic field amplitudes, with $f = 37$ kHz, as illustrated in Figure 2E. Here, 120 °C is the temperature for the LCE to reach 40% actuation strain (see Figure S1, Supporting Information, for the strain versus temperature curve of the LCE). The objective is to reach 120 °C for the top LM square under $B_1 = 9.6$ mT, then for the top two LM squares under $B_2 = 19.2$ mT, and finally for all three LM squares, under $B_3 = 28.8$ mT. To
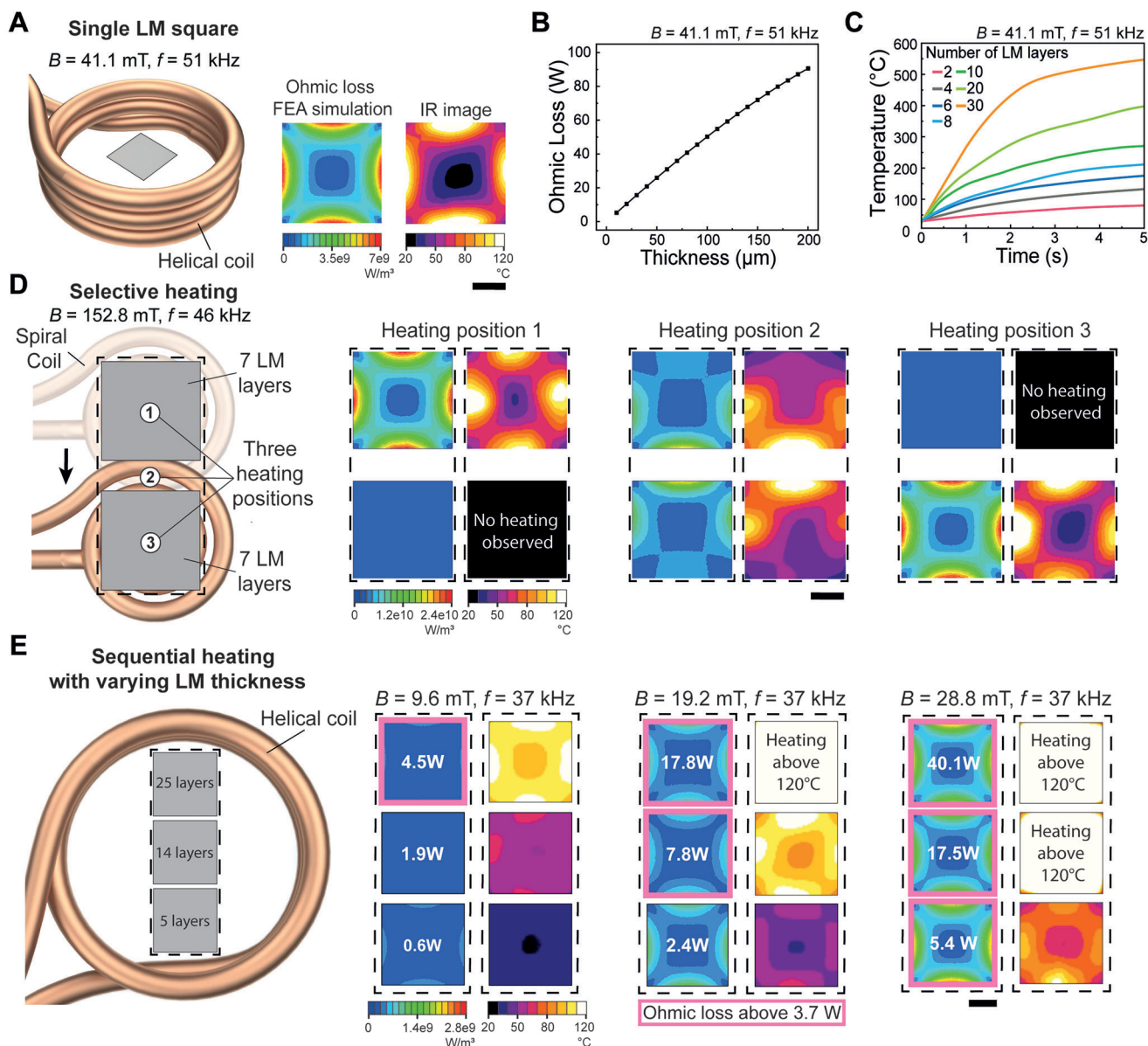
**ADVANCED
SCIENCE NEWS**

www.advancedsciencenews.com

**ADVANCED
MATERIALS**

www.advmat.de

Figure 2. Characterizations of induction heating of LM squares (15 mm × 15 mm) for selective and sequential heating. A) Induction heating of a 10-layer LM square and its FEA-predicted ohmic loss distribution and measured temperature distribution under $B = 41.1$ mT and $f = 51$ kHz. B) Total ohmic loss of the LM versus LM thickness/number of LM layers. C) Measured temperature versus time for the LM with varied LM thickness/number of LM layers. D) Ohmic loss and measured temperature distribution during selective heating of two 7-layer LM squares when a coil is placed at three distinct positions labeled 1, 2, and 3 under $B = 152.8$ mT and $f = 46$ kHz. E) Ohmic loss and measured temperature distribution during sequential heating of three LM squares with varied numbers of layers (25, 14, 5 layers) under increasing magnetic field intensity at $f = 37$ kHz. Scale bars: 5 mm.

determine the number of LM layers for sequential heating, the specific heat equation is used to calculate the critical ohmic loss above which an LM square would be able to heat the LCE layers of the composite to 120 °C in less than 2 s. Based on the dimensions of the LM pattern and the LCE thermal properties, this critical ohmic loss is found to be 3.7 W (see specific heat calculations in Supporting Information for more details on the critical ohmic loss). Electromagnetic FEA simulations are then performed to determine the number of LM layers needed for the total ohmic loss of each square to reach 3.7 W, under the different magnetic field amplitudes. Based on this calculation, the three

squares (positioned vertically in Figure 2E) should consist of 25 (~250 μm thick), 14 (~140 μm thick), and 5 (~50 μm thick) layers, from top to bottom. It is seen that, when the magnetic field increases from 9.6 to 19.2 mT, and finally to 28.8 mT, the three squares are sequentially heated above 120 °C in three steps, starting from the top square with the highest number of LM layers, to the top two squares, and lastly to all three squares (see Movie S2, Supporting Information, for the sequential heating process). The demonstrated selective heating and sequential heating are further utilized for programmable deformation and motion in the following sections.
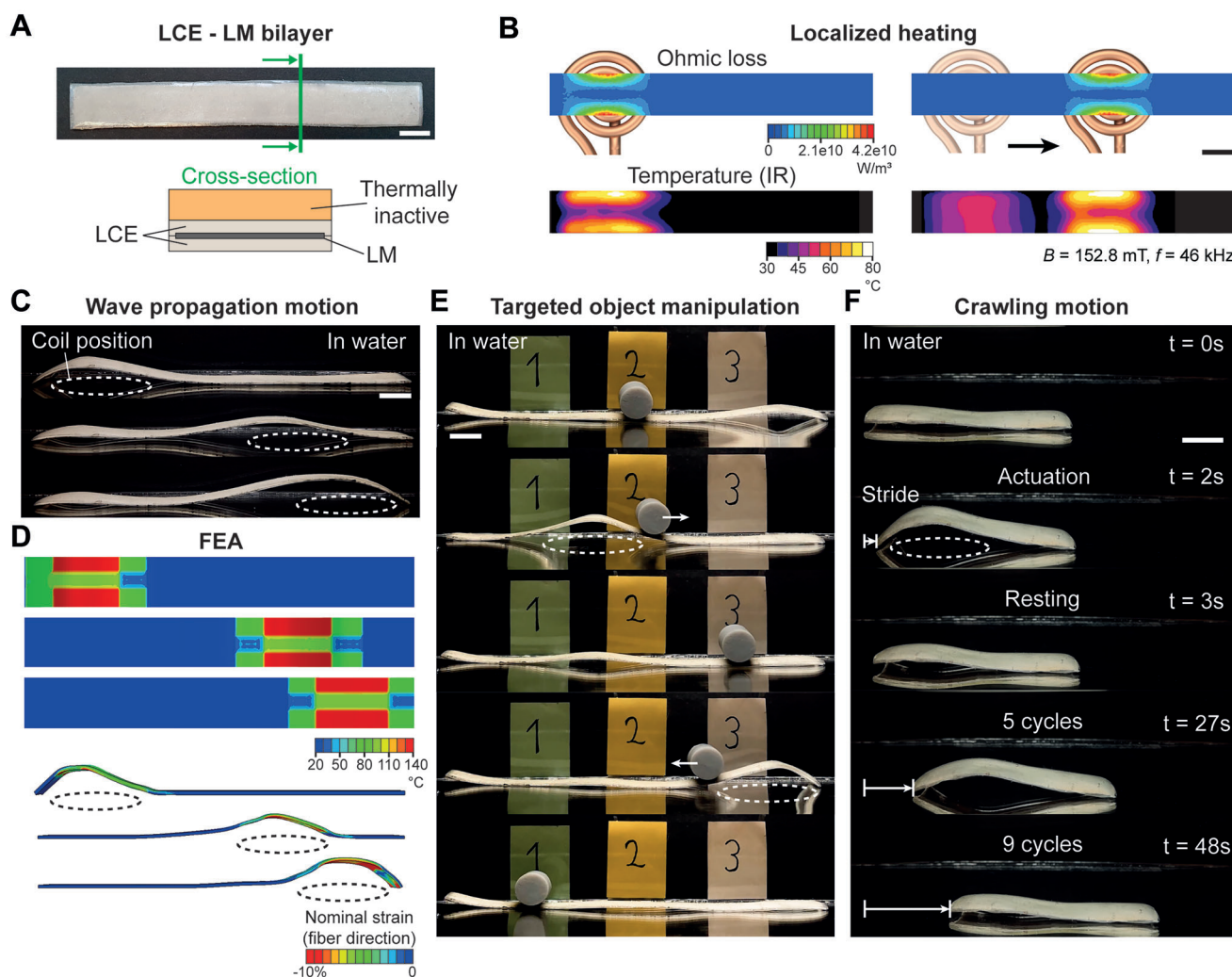
**ADVANCED
SCIENCE NEWS**

www.advancedsciencenews.com

**ADVANCED
MATERIALS**

www.advmat.de

Figure 3. In-water actuation of LCE-LM bilayer strips for wave propagation motion, object manipulation, and crawling. A) Fabricated sample and its material composition shown by the cross-section schematic. The sample consists of two LCE layers with longitudinally aligned mesogens and 6 layers of LM sandwiched in between. A thermally inactive material layer is bonded on top of the LCE-LM composite. Scale bar: 10 mm. B) Simulated ohmic loss distribution and measured temperature distribution of the LM locally heated by a spiral coil with $B = 152.8$ mT and $f = 46$ kHz. Scale bar: 10 mm. C) Wave propagation motion achieved by moving the coil underneath the sample in water. Scale bar: 10 mm. D) Temperature distribution in thermo-structural FEA and simulated wave propagation motion of the sample. E) In-water manipulation of a cylinder through programmed localized heating of the sample. Scale bar: 10 mm. F) In-water crawling motion through repeated heating and cooling of the sample. Scale bar: 15 mm.

2.3. In-Water Motion and Object Manipulation by Programmable Heating

The untethered induction heating of LM allows for fast, reversible actuations of the LCE in room-temperature water (measured to be 23 °C), which are otherwise challenging to accomplish with conventional LCE actuation strategies, such as joule heating, photothermal heating, or heat guns. The room-temperature water also provides fast cooling due to its high thermal conductivity and heat capacity compared to air. The easy repositioning of the magnetic field by moving the coil further enables the spatially programmable eddy current for controllable LCE motion and functionality in an aquatic environment, which has never been achieved with other heating methods before. To demonstrate the programmable in-water actuation, we fabricated an

LCE-LM bilayer, as shown in **Figure 3**A, composed of 6 LM layers (~60 μm thick) sandwiched between two LCE strips with mesogens aligned longitudinally by DIW. The top surface of the strips is then bonded with a layer of thermally inactive material (shear modulus 890 kPa, see Figure S1, Supporting Information, for the material characterizations), which causes the sample to bend when the LCE strips are actuated (see "Experimental Section" for details on the bilayer fabrication). Even though the LM pattern is a long rectangle, it is still very effective to actuate only a selected LCE region by applying a localized magnetic field, as the heat does not effectively propagate to the LM regions far from the field. As demonstrated in Figure 3B, the ohmic loss distribution (FEA predicted, see Supporting Information for the electromagnetic FEA) and the resulting high-temperature zone (IR measured) travels along the LCE strips with the moving coil, which

**ADVANCED
SCIENCE NEWS**

www.advancedsciencenews.com

**ADVANCED
MATERIALS**

www.advmat.de

generates an alternating magnetic field with $B = 152.8$ mT and $f = 46$ kHz (see Movie S3, Supporting Information, for the heat propagation IR video, see Figure S6, Supporting Information, for coil details). When actuated in water, the coil movement leads to a wave propagation motion, as illustrated in Figure 3C. The wave front moves simultaneously with the coil, demonstrating efficient heating even in cold water. The fast cooling of the sample enabled by water also allows for rapid motions (see Movie S3, Supporting Information, for the in-water actuation of the bilayer). As shown in Figure 3D, this wave motion is also well captured by thermo-structural FEA simulations. To model the bilayer bending, a nonuniform temperature distribution is imposed to replicate the temperature profile observed experimentally (see Figure S10, Supporting Information, and the thermo-structural FEA section in the Supporting Information for more details). The resulting bending deformation and wave propagation closely match the continuous motion observed in experiments (see Movie S3, Supporting Information, for the thermo-structural FEA simulated deformation).

This wave propagation motion is further utilized to precisely manipulate an object in water. As demonstrated in Figure 3E, the wave motion induced by the localized actuation of the LCE-LM bilayer strip accurately pushes a cylinder from one target position to another (see Movie S3, Supporting Information, for the targeted object manipulation). Finally, a crawling motion is achieved in water through the cyclic actuation of a shorter bilayer strip. As depicted in Figure 3F, for each actuation cycle of the crawler, the heat is localized on the left end of the sample, causing only the left part to bend and lift from the ground. The high friction of the undeformed right part of the crawler results in the bending-induced contraction of the sample. The coil is then moved to the right, and the recovering motion of the left part pushes the whole body to translate to the right. After nine cycles of reversible bending deformation, the crawler moves by approximately half of its body length in less than 1 min (see Movie S3, Supporting Information, for the crawling motion). In summary, spatially programmable eddy current induction heating coupled with the fast cooling enabled by water enables agile motions of the LCE, leading to controllable aquatic object manipulation and crawling.

2.4. Sequential Actuation of a Pop-Up Structure

As discussed above, the intensity of eddy current can also be spatially programmed for sequential actuation of the LCE-LM composite by prescribing the LM thickness distribution in the specimen. In this section, a sequential popping-up motion is demonstrated by designing regions with different numbers of LM layers. **Figure 4**A shows the fabricated LCE-LM circular disk with mesogens aligned circumferentially by DIW. To show the sequential actuation, the circular disk is divided into two LM pattern regions: an inner LM circle and an outer segmented LM ring. The inner LM circle is designed to produce a higher ohmic loss than the outer LM ring segments under the same magnetic field. To calculate the desired number of LM layers for the inner and outer LM regions, we evaluate the FEA-predicted total ohmic loss of each pattern to be above the critical ohmic loss for a temperature increase higher than 120 °C in less than 2 s (see specific heat calculations in Supporting Information for more details on

the critical ohmic loss). It can be seen in Figure 4B that, based on these calculations, the inner LM circle is made of 20 LM layers (~200 µm thick), and the segmented outer LM ring of 6 LM layers (~60 µm thick) to enable sequential heating of the structure under two different magnetic field amplitudes. The LM is sandwiched between a thinner bottom and a thicker top circular LCE layer (see "Experimental Section" for the pop-up structure fabrication). The thickness difference between the two LCE layers enables the bending in a prescribed direction since the thinner LCE layer heats faster and contracts more when the structure is actuated. As illustrated in Figure 4C, the pop-up structure is heated by a spiral coil (see Figure S8, Supporting Information, for coil details), with $f = 60$ kHz. The structure is placed on a substrate above the coil. The inner LM circle and the outer LM ring patterns are highlighted by green and purple dashed lines, respectively, along with two reference points, point A (red) and point B (blue), which are used to measure the deformation of the structure throughout its actuation.

To achieve sequential heating, the magnetic field is first gradually ramped up to $B = 13.1$ mT with $f = 60$ kHz, under which the ohmic loss distribution induces efficient heating to actuate only the inner LM circle region of the LCE structure. This sequential actuation is explained by the ohmic loss and IR temperature measurement shown in Figure 4D. As depicted in this figure, the FEA-predicted total ohmic loss (see Supporting Information for the electromagnetic FEA) in the inner LM circle is higher than it is in the outer LM ring segments, with values of 3.88 and 0.73 W, respectively. To heat the LCE above 80 °C (15% strain) to generate visible deformations in less than 2 s, the critical ohmic loss is calculated as 1.3 W. It is then demonstrated that only the inner LM circle is able to heat and actuate the LCE layers above 80 °C, while the outer ring segments fail to heat the LCE layers to the same extent (see specific heat calculations in Supporting Information for more details on the critical ohmic loss, and Figure S1, Supporting Information, for the strain versus temperature curve of the LCE). This is also confirmed by the IR measurements. As shown in Figure 4E, upon increasing the magnetic field amplitude to $B = 42.6$ mT under the same frequency, the total ohmic loss increases to 40.97 W in the inner LM circle, and to 7.71 W in the outer LM segmented ring, which are both above the critical ohmic loss value of 2.2 W to heat the LCE layers to 120 °C (40% strain) for large shape change in less than 2 s (see Figure S1, Supporting Information, for the strain versus temperature curve of the LCE, see specific heat calculations in Supporting Information for more details on the critical ohmic loss). The temperatures are confirmed by the IR measurements. Through this two-step actuation, sequential popping-up deformations are obtained with this circular LCE-LM composite with programmed LM thickness distribution. To predict the sequential deformation, we adopt the measured temperature observed in the sample at the two magnetic field amplitudes and input them to the thermo-structural FEA. The simulated temperature distributions shown in Figure 4D,E are from the heat transfer process. The comparison between the simulated sequential pop-up behavior and the actual actuation is shown in Figure 4F, demonstrating excellent agreement (see Movie S4, Supporting Information, for the thermo-structural FEA and experiment). The initial state, first actuated state, and final actuated state of the structure are shown in Figure 4F-i–iii, corresponding to $B = 0$, 13.1, and

**ADVANCED
SCIENCE NEWS**

www.advancedsciencenews.com
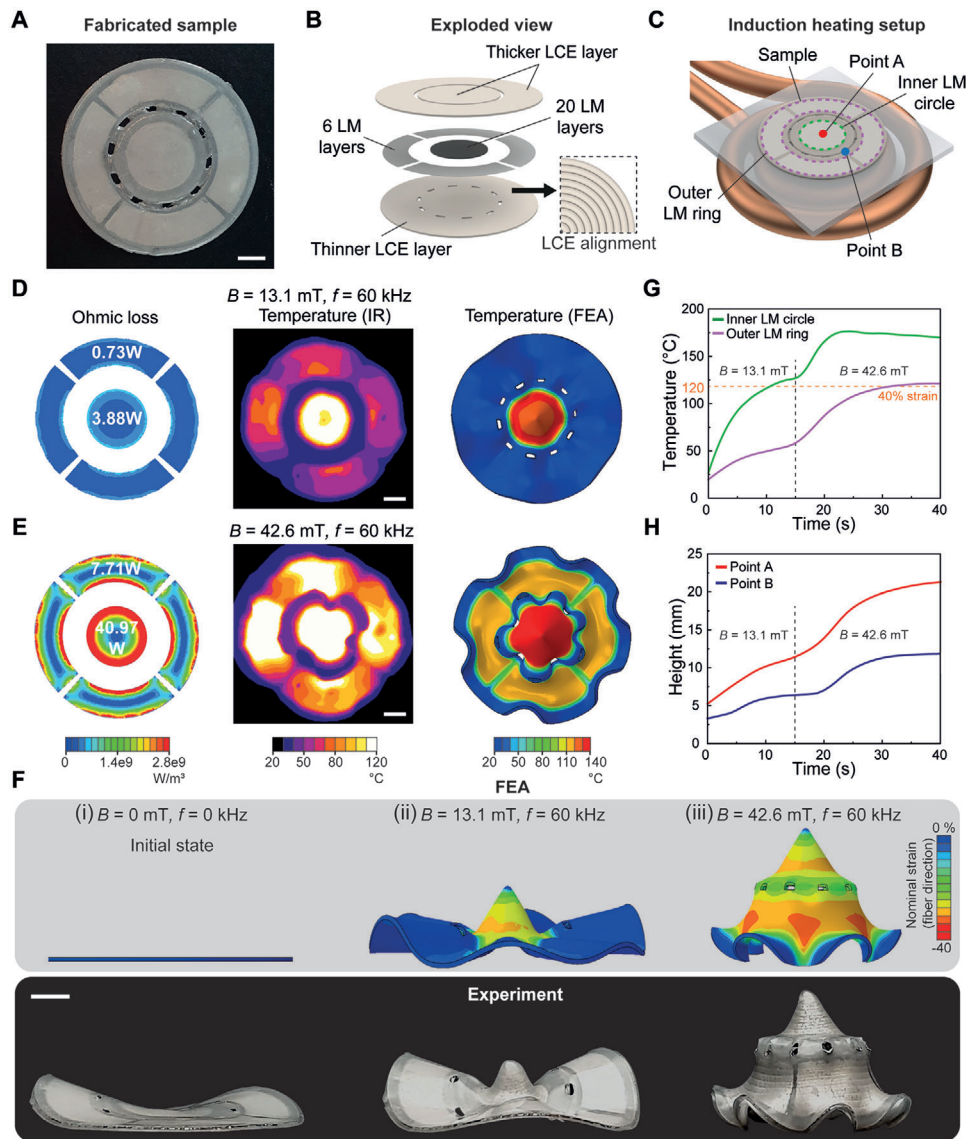
**ADVANCED
MATERIALS**

www.advmat.de

Figure 4. Pop-up LCE-LM structure and its sequential actuation. A) Fabricated sample. Scale bar: 5 mm. B) Exploded view of the sample, with a 20-layer LM circle for the inner LCE circle and a 6-layer segmented LM ring for the outer LCE ring. The LCE layers have circumferential mesogen alignment. C) Induction heating setup. The sample is placed on a substrate laying on a spiral coil. Two reference points, point A and point B, as well as a schematic of the inner LM circle and the outer LM ring are highlighted on the sample. Simulated ohmic loss distribution FEA, measured temperature distribution, and temperature distribution in thermo-structural FEA for D) $B = 13.1$ mT and $f = 60$ kHz, and E) $B = 42.6$ mT and $f = 60$ kHz. Scale bars: 5 mm. F) Sequential actuation (thermo-structural FEA and experiment) under the three magnetic field amplitudes i) $B = 0$ mT, ii) $B = 13.1$ mT, and iii) $B = 42.6$ mT. Scale bar: 5 mm. G) Temperature versus time for the inner LM circle (green) and the outer LM ring (purple). The vertical black dashed line denotes the time at which the magnetic field is increased from 13.1 to 42.6 mT. The horizontal orange dashed line represents 120 °C, which generates 40% strain of the LCE. H) Height at points A (red) and B (blue) versus time during actuation. The vertical black dashed line denotes the time at which the magnetic field is increased from 13.1 to 42.6 mT.

42.6 mT, respectively. For details on the thermo-structural FEA, see the thermo-structural FEA section in the Supporting Information. It is also worth noting that the slightly non-flat initial state of the structure is attributed to the residual stress during sample fabrication. This initial state does not affect the sequential actuation, due to the large contraction of LCEs.

To characterize the temperature evolution in the different regions of the structure, the temperature at the center of the inner LM circle and the average temperature of the centers of the

outer LM segments are recorded during heating by IR imaging, as illustrated by the green and purple curves in Figure 4G, respectively. It is seen that under $B = 13.1$ mT, the structure is actuated only in the inner LM circle region within the first 10 s of heating. The temperature achieved in this region surpasses 120 °C, corresponding to 40% strain of the LCE, (denoted by the orange dashed line, see Figure S1, Supporting Information, for the strain vs temperature curve of the LCE) and thus enables full contraction along the LCE fiber direction, and a significant
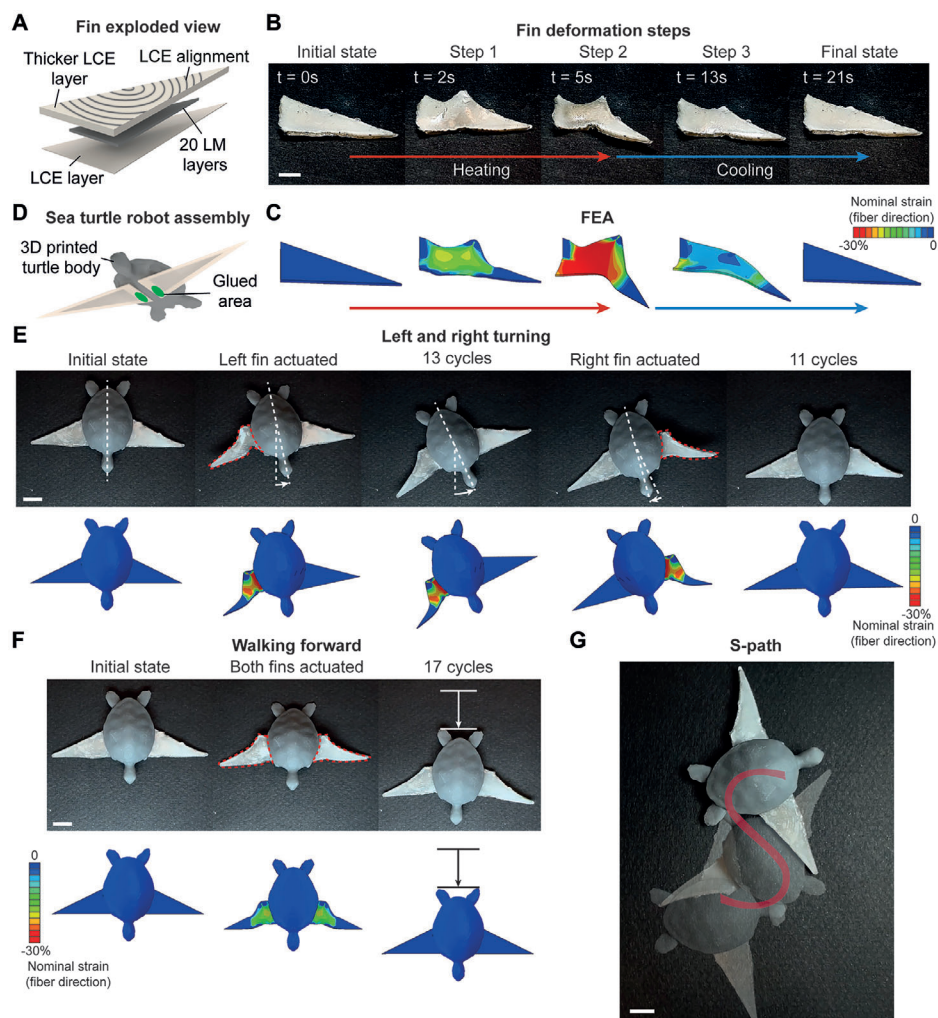
**ADVANCED
SCIENCE NEWS**

www.advancedsciencenews.com

**ADVANCED
MATERIALS**

www.advmat.de

Figure 5. Actuation and omnidirectional motion of the LCE-LM robotic sea turtle. A) Exploded view of an LCE-LM fin. The fin consists of 20-layer LM sandwiched between one thicker and one thinner LCE layer. The mesogen alignment of the LCE is circular. B) Fin actuation process. Scale bar: 5 mm. C) Fin deformation predicted by thermo-structural FEA. D) Schematic of the sea turtle assembly. The fins are glued onto the turtle body at the green zones. E) Sea turtle turning motion experiment (top) and thermo-structural FEA prediction (bottom), F) walking motion experiment (top) and thermo-structural FEA (bottom), and G) combined walking and turning motion of the sea turtle to follow an "S"-shaped path. The applied magnetic field is $B = 107.4$ mT and $f = 37$ kHz. Scale bars: 7 mm.

actuation of the inner section of the structure, which is demonstrated by the side view in Figure 4F-ii. On the other hand, the outer LM ring temperature plateaus around 50 °C, which is insufficient to trigger large LCE deformation. However, when the magnetic field is increased to $B = 42.6$ mT at 15 s, both the inner LM circle and the outer LM ring surpass 120 °C, allowing the whole structure to be fully actuated, as demonstrated by the side view in Figure 4F-iii. The deformation of the sample at different positions is then quantitatively measured and presented in Figure 4H, in which the elevation of point A and point B are recorded during the popping-up of the structure, as illustrated by the red and blue curves, respectively. For $B = 13.1$ mT, the inner LM circle region, represented by point A, elevates at a higher rate compared to the outer LM ring region, represented by point B. However, when B is increased to 42.6 mT, the heights of both A and B increase significantly (see Movie S4, Supporting Information, for the pop-up deformation). The sequential popping-up of

the LCE-LM structure therefore shows the easy programming of multimodal deformation by designing the LM heating efficiency through its thickness distribution.

2.5. Robotic Sea Turtle with Omnidirectional Locomotion

In this section, we design a soft robot capable of controllable omnidirectional crawling to mimic the motion of a sea turtle through the actuation of LCE-LM "fins". The turtle robot consists of a 3D-printed rigid body driven by two soft LCE-LM fins. In nature, a sea turtle uses its fin to generate a rotational deformation at the fin joint with an out-of-plane bending, leading to a pushing forward motion. To mimic this motion, we design LCE fins (**Figure 5**A) with circularly aligned LCE sheets to enable a joint-like rotation around the center of the LCE circular alignment during contraction. To generate the out-of-plane bending, the fins

**ADVANCED
SCIENCE NEWS**

www.advancedsciencenews.com

**ADVANCED
MATERIALS**

www.advmat.de

are designed with a thicker top and a thinner bottom LCE sheet to create a non-uniform heating distribution inside the fin. 20 LM layers (~200 µm thick) are sandwiched between the two LCE sheets. When actuated, the fins undergo a series of deformation steps as illustrated in Figure 5B (see Movie S5, Supporting Information, for the fin deformation). Upon induction heating, the LCE sheets contract around the center of the circular alignment in a joint-like rotation. At the first actuation step, the temperature distribution in the LCE sheets is asymmetric due to their thickness difference, causing the bending of the fins, which, combined with the rotational deformation, generates a pushing motion capable of driving the turtle's movement. As the heating increases, the fins reach their second deformation step, at which they are now fully actuated with the maximum contraction strain. This causes the rotational deformation of the fin to occur in a plane almost parallel to the substrate. When cooling down, the fins do not follow the same deformation steps as when they are heated, which is shown by the third deformation step. The fins do not bend but simply rotate their tips back around the joint to their initial positions. Due to their asymmetric deformation during heating and cooling, the fins are able to generate translational motion to move the sea turtle. As shown in Figure 5C, these deformation steps are well captured by a thermo-structural FEA (see the thermo-structural FEA section in the Supporting Information for more details).

To demonstrate the turtle motion, two triangular fins are glued to a 3D-printed rigid turtle body (Figure 5D, see "Experimental Section" for the sea turtle fabrication). A turning motion is achieved by selectively actuating one fin at a time (Figure 5E), while a simultaneous actuation of both fins leads to a forward motion (Figure 5F). As detailed in Figure 5E, we demonstrate the turtle turning motion by repeatedly actuating the left fin, and then the right fin, with a local magnetic field of amplitude $B = 107.4$ mT and frequency $f = 37$ kHz (see Figure S4, Supporting Information, for coil details). This turning motion is very well predicted by the thermo-structural FEA, in which a temperature of 140 °C is imposed in the fins (see Movie S5, Supporting Information, for the turning motion, see the thermo-structural FEA section in the Supporting Information for more details on the simulations). The forward motion of the turtle is achieved by actuating both fins using a larger coil that provides a magnetic field spatially covering the two fins, with $B = 107.4$ mT, and $f = 37$ kHz (see Figure S4, Supporting Information, for coil details). The turtle is capable of walking along a straight line, as shown in Figure 5F, with good agreement between the thermo-structural FEA and experiment (see Movie S5, Supporting Information, for the walking motion). Finally, as shown in Figure 5G, an "S"-shaped crawling path is realized by coupled turning and straight walking motion, demonstrating the turtle's ability to perform omnidirectional motion (see Movie S5, Supporting Information, for the "S"-shaped path).

3. Conclusion

In summary, we have reported an LCE-LM composite capable of ultrafast, untethered, and programmable LCE actuations by utilizing LM induction heating. By moving the magnetic field and varying the LM thickness and field strength, the eddy current is locally tuned, allowing for selective and sequential heating of the composite. Combined with DIW, which allows for the easy programming of the mesogen alignment direction, this LM induction heating actuation strategy is capable of complex LCE pop-up deformation, omnidirectional robotic motion, and in-water targeted object manipulation and crawling. Coupled with simulation tools for designing and predicting the composite actuations, we anticipate that the LCE-LM composite will not only expand the application possibilities of LCEs but also inspire new designs and actuation strategies for other temperature-driven actuators.

4. Experimental Section

LCE-LM Composite Fabrication: To fabricate the LCE ink, the mesogens (2-Methyl-1,4-phenylene bis(4-((6-(acryloyloxy)hexyl)oxy)benzoate)) (RM 82, BOC Sciences, USA) and (1,4-Bis-[4-(3-acryloyloxypropyloxy)benzoyloxy]-2-methylbenzene) (RM 257, BOC Sciences, USA) were mixed in a weight ratio of 3:1. The spacers (2,2-(Ethylenedioxy)diethanethiol) (EDDET, Sigma Aldrich, USA) and (2,6-Di-tert-butyl-4-methylphenol) (BHT, Sigma Aldrich, USA) were then introduced with 25 and 2 wt%, respectively, compared to the total weight of mesogens. After melting all the components at 80 °C for 1 h, the catalyst triethylamine (TEA, Sigma Aldrich, USA) and the photoinitiator Irgacure 819 (Sigma Aldrich, USA) were added to the mixture with 1 and 2 wt%, respectively, compared to the total weight of mesogens. The mixture was then stirred for 3 min with a magnetic stir bar at 80 °C for homogenization and oligomerized in an oven at 80 °C for 25 min. The mixture was next transferred to a 10 mL syringe barrel (Nordson EFD, USA), and heated again in a vacuum oven at 80 °C for 20 min. The ink was finally defoamed in a planetary mixer (AR-100, Thinky, USA) at 2200 rpm for 3 min to remove trapped air.

For the printing of LCEs, the syringe barrel filled with LCE ink was mounted to a customized 3D printer. The air pressure to the barrel was individually powered by a high-precision dispenser (Ultimus V, Nordson EFD, USA). The material was printed at room temperature at a speed of 15 mm s^{-1} and pressure of 550 kPa to align the LCE mesogens along the print path for large strains. The needle used had 0.58 mm inner diameter (Smoothflow tapered dispense tips 7005009, Nordson EFD, USA). The distance from the syringe needle to the printing substrate was 0.2 mm, and the distance from two neighboring printed filaments was set to 0.35 mm. To fix the printed filaments for further steps, the LCE was cured by UV light (385 nm) for 15 s after printing.

Once the first LCE layer was printed with the desired shape and alignment direction, the LCE layer was covered with a laser-cut paper mask (K40 CO2 laser, OMTech Laser Inc., USA) for the desired LM pattern. The LM (Galinstan, Rotometals Inc., USA) was then sprayed onto the LCE layer using an airbrush paint sprayer (Master Airbrush, USA) at a pressure of 1.5 bar. To apply a specific thickness of LM, the spraying procedure was normalized by defining "LM layers", with one layer corresponding to ~10 µm thickness (see Figure S9, Supporting Information, for the relationship between the thickness and the number of LM layers sprayed). After spraying LM layers for the desired thickness, the mask was removed, and another LCE layer printed separately was placed on top. Light pressure was then applied in the zones where the LCE layers were in direct contact to bond the two LCE layers together. No pressure was applied on the LM region during the sealing of the LCE-LM composite. The LCE-LM composite was finally processed with UV light (385 nm) for 10 min to fully cure the two LCE layers and firmly bond them together (see Figure S2, Supporting Information, for more details on the composite fabrication, see Figure S3, Supporting Information, for the interfacial adhesion characterization of the composite).

LCE Disks with an LM Ring and an LM Circle Fabrication: To fabricate the LCE disks demonstrated in Figure 1E,F, two circular LCE layers of 45 mm diameter were printed with circumferentially aligned mesogens. After printing, the layers were cured with UV light (385 nm) for 10 min. 6 Layers (~60 µm thick) of LM were then sprayed using a paper mask de-

pending on the LM pattern. The LM ring pattern had an inner diameter of 23 mm and an outer diameter of 35 mm, and the LM circle had a diameter of 25 mm.

LCE-LM Bilayer Fabrication: To fabricate the LCE-LM bilayer demonstrated in Figure 3, an LCE-LM composite was made following the method described in *LCE-LM composite fabrication*. The long LCE strips of the LCE-LM bilayer in Figure 3A–E are rectangles of 120 mm × 15 mm × 0.15 mm in size, while the short LCE strips of the LCE-LM bilayer in Figure 3F are rectangles of 75 mm × 15 mm × 0.15 mm in size. For each composite, the 6-layer (~60 μm thick) LM pattern had a rectangular shape which was offset by 1.5 mm from every edge of the LCE layers. To obtain the bending deformation, the composite was covered by a thermally inactive photocurable material layer (Elastic 50A Resin, Formlabs Inc., USA) by spin-coating it at 600 rpm for 6 s. To fix the whole structure together, UV light (385 nm) was shined for 10 min onto the LCE-LM bilayer.

Pop-Up Structure Fabrication: For the pop-up structure, the top LCE layer consisted of an LCE circle of 15 mm diameter, and an LCE ring of 17.5 mm inner diameter and 35 mm outer diameter. The top layer was printed with a thickness of 0.2 mm by adjusting the nozzle height to 0.25 mm above the substrate and reducing the printing speed to 12 mm s^{-1}. The bottom LCE layer was made of the same LCE circle and LCE ring but connected by ten 3 mm wide segments arranged in an evenly spaced circular pattern. The bottom layer was printed with a thickness of 0.15 mm by using the printing parameters described in the *LCE-LM composite fabrication* section. Once the LCE layers were printed, both layers were cured with UV light (385 nm) for 15 s. The bottom LCE layer was then sprayed with LM. The inner LM circle denoted in Figure 4C was of 12 mm outer diameter and consisted of 20 layers (~200 μm thick) of LM. The outer LM ring denoted in Figure 4C was made of four circular segments of 19 mm inner diameter and 31 mm outer diameter arranged in an evenly spaced circular pattern, and the segments consisted of 6 layers (~60 μm thick) of LM. After spraying, the top LCE layer was placed on the bottom LCE layer, and UV light (385 nm) was finally shined for 10 min on the structure to firmly fix it together.

Sea Turtle Fabrication: To create the sea turtle fins, LCE-LM composites were made following the same method described in *LCE-LM composite fabrication*. The LCE layers were right triangles of size 15 mm × 25 mm with 0.45 mm thickness for the top layer, and 0.15 mm thickness for the bottom layer. The thicker layer was made from three 0.15 mm thick LCE layers. The LCE mesogen alignment was circular for both the bottom and the top LCE layers, and the alignment center was positioned on the longest triangle edge and was located at 8 mm from the shorter edge of the triangle. The LM pattern was also a right triangle offset by 1.5 mm from every edge of the LCE layers and consisted of 20 layers of LM (~200 μm thick). To cure the fins, UV light (385 nm) was shined for 10 min. The two fins were then fixed onto a 3D-printed sea turtle body (Grey Resin, Formlabs Inc., USA) by applying a thermally inactive photocurable material (Elastic 50A Resin, Formlabs Inc., USA) onto the regions green highlighted in Figure 5D. UV light (385 nm) was shined on the glued area for 10 min to bond the fins and the sea turtle body together.

Induction Heating: The LM patterns were inductively heated by applying external high-frequency alternating magnetic fields. To achieve the effective heating and associated actuation performance of the LCE-LM composites, five different water-cooled coils made by hollow copper tubes were connected to a LH-15 A induction heater (MXBAOHENG, China) to generate the alternating magnetic fields with different distributions and frequencies. By adjusting the currents supplied to the coils, the amplitudes of the magnetic fields were accurately tuned. The photos and magnetic field distributions of these coils are illustrated in Figures S4–S8 (Supporting Information). The detailed parameters of these coils are summarized in Table S1 (Supporting Information).

Supporting Information

Supporting Information is available from the Wiley Online Library or from the author.

Conflict of Interest

The authors declare no conflict of interest.

Author Contributions

R.Z. designed the research; V.M., Y.C., Q.Z., S.L, and J.W. performed the research; V.M., S.L., and J.W. carried out the experiments and analyzed the data; Y.C., S.L., and Q.Z. realized the FEA simulations; R.Z., V.M., Y.C., Q.Z., and S.L. wrote the paper. V.M. and Y.C. contributed equally to this work.

Data Availability Statement

The data that support the findings of this study are available from the corresponding author upon reasonable request.

[1] Q. Ze, S. Wu, J. Nishikawa, J. Dai, Y. Sun, S. Leanza, C. Zemelka, L. S. Novelino, G. H. Paulino, R. R. Zhao, *Sci. Adv.* **2022**, *8*, 7834.

[2] W. Hu, G. Z. Lum, M. Mastrangeli, M. Sitti, *Nature* **2018**, *554*, 81.

[3] A. Kotikian, J. M. Morales, A. Lu, J. Mueller, Z. S. Davidson, J. W. Boley, J. A. Lewis, *Adv. Mater.* **2021**, *33*, 2101814.

[4] Q. Ze, X. Kuang, S. Wu, J. Wong, S. M. Montgomery, R. Zhang, J. M. Kovitz, F. Yang, H. J. Qi, R. Zhao, *Adv. Mater.* **2020**, *32*, 1906657.

[5] R. Guo, X. Sun, B. Yuan, H. Wang, J. Liu, *Adv. Sci.* **2019**, *6*, 1901478.

[6] P. Lavrador, M. R. Esteves, V. M. Gaspar, J. F. Mano, *Adv. Funct. Mater.* **2021**, *31*, 2005941.

[7] H. Zeng, O. M. Wani, P. Wasylczyk, R. Kaczmarek, A. Priimagi, *Adv. Mater.* **2017**, *29*, 1701814.

[8] A. Ghosh, L. Li, L. Xu, R. P. Dash, N. Gupta, J. Lam, Q. Jin, V. Akshintala, G. Pahapale, W. Liu, A. Sarkar, R. Rais, D. H. Gracias, F. M. Selaru, *Sci. Adv.* **2020**, *6*, 4133.

[9] Q. Zhao, H. J. Qi, T. Xie, *Prog. Polym. Sci.* **2015**, *49–50*, 79.

[10] W. Miao, W. Zou, B. Jin, C. Ni, N. Zheng, Q. Zhao, T. Xie, *Nat. Commun.* **2020**, *11*, 4257.

[11] A. Lendlein, O. E. C. Gould, *Nat. Rev. Mater.* **2019**, *4*, 116.

[12] Y. S. Zhang, A. Khademhosseini, *Science* **2017**, *356*, 3627.

[13] H. Yuk, S. Lin, C. Ma, M. Takaffoli, N. X. Fang, X. Zhao, *Nat. Commun.* **2017**, *8*, 14230.

[14] D. Morales, E. Palleau, M. D. Dickey, O. D. Velev, *Soft Matter* **2014**, *10*, 1337.

[15] X. Kuang, S. Wu, Q. Ze, L. Yue, Y. Jin, S. M. Montgomery, F. Yang, H. J. Qi, R. Zhao, *Adv. Mater.* **2021**, *33*, 2102113.

[16] G. Z. Lum, Z. Ye, X. Dong, H. Marvi, O. Erin, W. Hu, M. Sitti, *Proc. Natl. Acad. Sci. U. S. A.* **2016**, *113*, E6007.

[17] Y. Kim, H. Yuk, R. Zhao, S. A. Chester, X. Zhao, *Nature* **2018**, *558*, 274.

[18] H. Aharoni, Y. Xia, X. Zhang, R. D. Kamien, S. Yang, *Proc. Natl. Acad. Sci. U. S. A.* **2018**, *115*, 7206.

[19] S. W. Ula, N. A. Traugutt, R. H. Volpe, R. R. Patel, K. Yu, C. M. Yakacki, *Liq. Cryst. Rev.* **2018**, *6*, 78.

[20] K. M. Herbert, H. E. Fowler, J. M. McCracken, K. R. Schlafmann, J. A. Koch, T. J. White, *Nat. Rev. Mater.* **2022**, *7*, 23.

[21] A. Buguin, M. H. Li, P. Silberzan, B. Ladoux, P. Keller, *J. Am. Chem. Soc.* **2006**, *128*, 1088.

[22] H. Wermter, H. Finkelmann, *e-Polymers* **2001**, *1*, 013.

[23] T. H. Ware, M. E. McConney, J. J. Wie, V. P. Tondiglia, T. J. White, *Science* **2015**, *347*, 982.

[24] X. Peng, S. Wu, X. Sun, L. Yue, S. M. Montgomery, F. Demoly, K. Zhou, R. R. Zhao, H. J. Qi, *Adv. Mater.* **2022**, *34*, 2204890.

[25] Y. Xia, G. Cedillo-Servin, R. D. Kamien, S. Yang, *Adv. Mater.* **2016**, *28*, 9637.

[26] M. Wang, Z. W. Cheng, B. Zuo, X. M. Chen, S. Huang, H. Yang, *ACS Macro Lett.* **2020**, *9*, 860.

[27] Y. Li, H. Yu, K. Yu, X. Guo, X. Wang, *Adv. Funct. Mater.* **2021**, *31*, 2100338.

[28] D. L. Thomsen, P. Keller, J. Naciri, R. Pink, H. Jeon, D. Shenoy, B. R. Ratna, *Macromolecules* **2001**, *34*, 5868.

[29] H. F. Jürgen Küpfer, *Macromol. Rapid Commun.* **1991**, *12*, 717.

[30] T. Guin, M. J. Settle, B. A. Kowalski, A. D. Auguste, R. V. Beblo, G. W. Reich, T. J. White, *Nat. Commun.* **2018**, *9*, 2531.

[31] T. A. Kent, M. J. Ford, E. J. Markvicka, C. Majidi, *Multifunct Mater* **2020**, *3*, 025003.

[32] Q. He, Z. Wang, Y. Wang, A. Minori, M. T. Tolley, S. Cai, *Sci. Adv.* **2019**, *5*, 5746.

[33] Y. Yang, Z. Pei, Z. Li, Y. Wei, Y. Ji, *J. Am. Chem. Soc.* **2016**, *138*, 2118.

[34] H. Kim, J. A. Lee, C. P. Ambulo, H. B. Lee, S. H. Kim, V. V. Naik, C. S. Haines, A. E. Aliev, R. Ovalle-Robles, R. H. Baughman, T. H. Ware, *Adv. Funct. Mater.* **2019**, *29*, 1905063.

[35] L. Qin, X. Liu, Y. Yu, *Adv. Opt. Mater.* **2021**, *9*, 2001743.

[36] A. Kotikian, R. L. Truby, J. W. Boley, T. J. White, J. A. Lewis, *Adv. Mater.* **2018**, *30*, 1706164.

[37] Z. Wang, Z. Wang, Y. Zheng, Q. He, Y. Wang, S. Cai, *Sci. Adv.* **2020**, *6*, 0034.

[38] S. Wu, Y. Hong, Y. Zhao, J. Yin, Y. Zhu, *Sci. Adv.* **2023**, *9*, 8014.

[39] M. Rogóż, H. Zeng, C. Xuan, D. S. Wiersma, P. Wasylczyk, *Adv. Opt. Mater.* **2016**, *4*, 1689.

[40] L. Wang, M. Y. Razzaq, T. Rudolph, M. Heuchel, U. Nöchel, U. Mansfeld, Y. Jiang, O. E. C. Gould, M. Behl, K. Kratz, A. Lendlein, *Mater. Horiz.* **2018**, *5*, 861.

[41] H. Wei, Q. Zhang, Y. Yao, L. Liu, Y. Liu, J. Leng, *ACS Appl. Mater. Interfaces* **2017**, *9*, 876.

[42] Q. Wang, C. Pan, Y. Zhang, L. Peng, Z. Chen, C. Majidi, L. Jiang, *Matter* **2023**, *6*, 855.

[43] A. Kaiser, M. Winkler, S. Krause, H. Finkelmann, A. M. Schmidt, *J. Mater. Chem.* **2009**, *19*, 538.

[44] Y. Wu, S. Zhang, Y. Yang, Z. Li, Y. Wei, Y. Ji, *Sci. Adv.* **2022**, *8*, 6021.

[45] T. Daeneke, K. Khoshmanesh, N. Mahmood, I. A. De Castro, D. Esrafilzadeh, S. J. Barrow, M. D. Dickey, K. Kalantar-Zadeh, *Chem. Soc. Rev.* **2018**, *47*, 4073.

[46] C. Zhang, X. Lu, G. Fei, Z. Wang, H. Xia, Y. Zhao, *ACS Appl. Mater. Interfaces* **2019**, *11*, 44774.

[47] C. P. Ambulo, J. J. Burroughs, J. M. Boothby, H. Kim, M. R. Shankar, T. H. Ware, *ACS Appl. Mater. Interfaces* **2017**, *9*, 37332.

[48] T. V. Neumann, B. Kara, Y. Sargolzaeiaval, S. Im, J. Ma, J. Yang, M. C. Ozturk, M. D. Dickey, *Micromachines* **2021**, *12*, 146.

[49] C. Guo, Y. Yu, J. Liu, *J. Mater. Chem. B* **2014**, *2*, 5739.

[50] M. D. Dickey, *Adv. Mater.* **2017**, *29*, 1606425.

[51] H. Wheeler, *Proc. IRE* **1942**, *30*, 299.

[52] E. H. Sondheimer, G. E. H. Reuter, *Proc. R. Soc. London, Ser. A* **1948**, *195*, 336.